Operando X-ray absorption spectroscopy applied to battery materials at ICGM
The challenging case of BiSb's sodiation

Darwiche, Ali; Murgia, Fabrizio; Fehse, Marcus; Mahmoud, Abdelfattah; Iadecola, Antonella; Belin, Stéphanie; La Fontaine, Camille; Briois, Valérie; Hermann, Raphael P.; More Authors

DOI
10.1016/j.ensm.2019.06.027

Publication date
2019

Document Version
Final published version

Published in
Energy Storage Materials

Citation (APA)
Darwiche, A., Murgia, F., Fehse, M., Mahmoud, A., Iadecola, A., Belin, S., La Fontaine, C., Briois, V., Hermann, R. P., & More Authors (2019). Operando X-ray absorption spectroscopy applied to battery materials at ICGM: The challenging case of BiSb's sodiation. *Energy Storage Materials*, *21*, 1-13. https://doi.org/10.1016/j.ensm.2019.06.027

Important note
To cite this publication, please use the final published version (if applicable).
Please check the document version above.

Energy Storage Materials 21 (2019) 1–13

Contents lists available at ScienceDirect

Energy Storage Materials

journal homepage: www.elsevier.com/locate/ensm

Operando X-ray absorption spectroscopy applied to battery materials at ICGM: The challenging case of BiSb's sodiation

Ali Darwiche [a], Fabrizio Murgia [a], Marcus Fehse [b,c,d], Abdelfattah Mahmoud [e], Antonella Iadecola [f], Stéphanie Belin [g], Camille La Fontaine [g], Valérie Briois [g], Raphael P. Hermann [h], Bernard Fraisse [a], Romain Berthelot [a,f,b], Moulay Tahar Sougrati [a,f,b], Laure Monconduit [a,f,b], Lorenzo Stievano [a,f,b,*]

[a] Institut Charles Gerhardt Montpellier (ICGM), Univ. Montpellier, CNRS, Montpellier, France
[b] Alistore European Research Institute, CNRS, Amiens, France
[c] Faculty of Applied Sciences, Delft University of Technology, Delft, Netherlands
[d] Dubble Beamline, European Synchrotron Research Facility (ESRF), Grenoble, France
[e] GreenMat, CESAM, Institute of Chemistry, Univ. Liège, Liège, Belgium
[f] Reseau sur le Stockage Electrochimique de l'Energie (RS2E), CNRS, Amiens, France
[g] Synchrotron Soleil, Gif-sur Yvette, France
[h] Material Science and Technology Division, Oak Ridge National Laboratory, Oak Ridge, USA

ARTICLE INFO

Keywords:
X-ray absorption spectroscopy
Batteries
Energy materials
Electrode materials
Electrochemical mechanism
Operando measurements

ABSTRACT

X-ray absorption spectroscopy (XAS) is a synchrotron-based, element-specific, short-range structural method largely used in the study of materials, already widely employed for the study of the electrochemical processes in battery systems. The high penetration of the X-rays makes XAS particularly suited for the study of battery materials under *operando* conditions using specifically developed *in situ* electrochemical cells. In this paper, the application of XAS to the study of battery materials carried out at Institut Charles Gerhardt Montpellier (France) will be outlined, illustrating the type of information provided by XAS. The challenging study of the sodiation of $Bi_{0.50}Sb_{0.50}$ followed individually and simultaneously at both metals will be also presented in order to highlight the typical advantages of this technique even when it is pushed at its technical limits.

1. Introduction

One of challenges that our society has to face is the sustainable use of energy. In particular, the demand for advanced energy storage devices has increased significantly, motivated by a variety of different needs of our technologically driven, highly mobile, energy-hungry society. Among the available technologies, electrochemical energy storage devices, *i.e.*, batteries, can provide the solution to the problems connected to the intrinsic intermittency of renewable energy sources, since they can buffer the energy surplus produced by the operating plant in periods of low consumption, and feed it back to the power grid in case of high demand [1]. Moreover, they can fulfill the ever growing demand of energy for portable applications (mobile phones and computers, and more recently electric vehicles). The excellent performance and the well-established technology of lithium-ion batteries (LIB) put them in a key position for supporting this new energy revolution [2]. Several post-LIB technologies, such as lithium-sulfur batteries (LSB) or sodium-ion batteries (NIB), have also been proposed in the last years, as viable performing alternatives to LIB.

Both LIBs and post-LIB systems are based on the so-called "rocking chair" mechanism, where Li^+ cations are exchanged alternatively between the positive and the negative electrode during cycling. In such a system, the two electrodes can be any sort of material that is able to undergo reversibly a reduction/oxidation process at a specific high or low potential (for the positive or negative electrode, respectively) with the concomitant addition/elimination of Li^+ cations. For this reason, a large number of different materials able to reversibly form lithiated phases via different reaction mechanisms, *i.e.*, intercalation [3–5], alloying [6–8], or conversion [9–12], have been proposed, thus generating a great deal of studies. In addition to the reaction mechanisms at the electrodes, other features concerning the electrolytes and their interaction with the electrodes, including the formation of the solid-electrolyte

* Corresponding author. Institut Charles Gerhardt Montpellier (ICGM), Univ. Montpellier, CNRS, Montpellier, France.
E-mail address: lorenzo.stievano@umontpellier.fr (L. Stievano).

https://doi.org/10.1016/j.ensm.2019.06.027
Received 31 January 2019; Received in revised form 14 June 2019; Accepted 19 June 2019
Available online 24 June 2019

interphase (SEI) [13], which is of primordial importance for the stability and the cycle life of the battery, have been thoroughly studied.

In such a picture, many characterisation techniques such as infrared [14–17], Raman [17–19], Mössbauer [20], X-ray absorption (XAS) [21–26] and X-ray photoelectron spectroscopy (XPS) [15,27,28] as well as X-ray diffraction (XRD) [29,30] have been largely applied, either *ex situ*, *in situ* or under *operando* conditions, for the characterisation of the pristine materials and of their reaction mechanisms. Among them, XAS remains a technique of choice for retrieving structural and electronic information, especially when the materials or some of the species formed through the electrochemical reactions are not crystalline and cannot be studied by diffraction techniques. The most important features of XAS are: (i) its element specificity, allowing the study of a single element by concentrating on its K (or in some cases L) absorption edge; (ii) the possibility of tuning it quasi-simultaneously to different sites (for instance Sn and Sb in SnSb) [31], thus providing sources of complementary information on the same compound; (iii) the physico-chemical information contained in the near-edge structure of the XAS signals, which can be used to reveal the formal oxidation state and the local symmetry of the probed atom; (iv) the possibility of performing measurements under *operando* conditions using specifically developed *in situ* electrochemical cells [32]. In this case, the physico-chemical properties and the local structure of the studied element can be monitored at all moments during the charge and discharge processes.

The application of XAS to the study of battery materials and their electrochemical reaction mechanisms has started several decades ago: to the best of our knowledge, the first paper on the application of XAS to the field of batteries was published by Mc Breen et al. [33] Many works have been published since that paper, resumed in different reviews which appeared over the years highlighting their principal results and advances [21–26]. In this paper, after a very short presentation of the technique and of the corresponding experimental methods, its potentialities will be highlighted going through its application to the study of battery materials at Institut Charles Gerhardt Montpellier (ICGM, France) in the last decade.

Finally, a challenging example of *operando* XAS to the study of the sodiation of $Bi_{0.50}Sb_{0.50}$ simultaneously at both Sb K-edge and Bi L_3 edge will be presented. This example will help us emphasize both the extremely advanced analytic capability of the ROCK beamline of Synchrotron Soleil (France) [34], probably the only beamline allowing continuous alternate measurements of XAS spectra of two elements with absorption edges at such different energies (Sb K-edge and Bi L_3-edge, 30491 and 13418 eV, respectively), as well as the use of chemometric methods for the analysis of the collected data. These findings perfectly complement the information gathered by *operando* XRD, allowing a precise description of the electrochemical mechanisms governing both Sb and Bi centres during a charge/discharge cycle.

2. Advantages and challenges of *operando* X-ray absorption spectroscopy: the work performed at ICGM

2.1. What is XAS?

XAS (sometimes abbreviated as XAFS for X-ray absorption fine structure) is an element-specific spectroscopic technique providing both chemical and structural information at the local scale (4–5 Å) about the probed element; for this reason, it is well suited for the characterisation of both crystalline and amorphous materials. The principles of XAS reside on the resonant absorption of X-rays generated by the photoelectric effect, *i.e.*, the photon-stimulated emission of electrons occurring when the energy of the incident photon equals or exceeds that of the ionisation energy of a specific electron, giving rise to an absorption edge. Depending on the probed element, the energy ranges from soft to hard X-rays regimes (0.2–40 keV).

XAS (or XAFS) generally refers to the entire spectrum, which is constituted by the edge region usually abbreviated as XANES (X-ray Absorption Near-Edge Structure), comprising the first 80–100 eV above the absorption edge, and a post-edge region usually abbreviated as EXAFS (Extended X-Ray Absorption Fine Structure), which usually extends to 1000 eV above the absorption edge.

The XANES region, comprising some pre-edge features and the absorption edge itself, is extremely sensitive to the oxidation state and to the coordination of the probed element. On the other hand, the periodic oscillations found in the EXAFS region, generated by the scattering of the emitted photoelectrons with the electrons of the neighbouring atoms, provide quantitative information about the nearest neighbours (bond distances, coordination number and nature of the bonding atoms).

XAS is very versatile and can be applied to all states of matter, from liquid to solids, crystalline or amorphous. It has been used with great success in many research fields, such as catalysis [35–39], biology [40,41], inorganic metal complexes [42], nanomaterials [43], and electrochemical interfaces [15,44]. Several excellent books are also available to obtain further detailed insights on the theory and on the applications of XAS [39,45–47]

2.2. Studies carried out at ICGM: anode and cathode insertion materials

In the last 10 years, most of the potentialities of XAS have been applied at ICGM to the study of batteries and battery materials. Having access to different synchrotron sources with complementary energy ranges and resolution, it was possible not only to fully profit of the advantages of this technique in studying several families of electrode materials, but also to extend its capabilities to the study of extremely complicated and challenging systems, improving the strategies for data analysis by applying specific advanced chemometric tools. This advanced approach allowed us, in some specific cases such as the reversible sodiation of antimony [48], to reach the limits of its sensitivity, demonstrating that XAS is intrinsically unable to observe the formation of some of the intermediates of the electrochemical reaction.

The development of *operando* XAS was made possible thanks to the previous work of Leriche et al., who designed, in collaboration with the team of beamline SAMBA at Synchrotron Soleil (now working at the more recent beamline ROCK, specialised on *operando* XAS), a new efficient *in situ* electrochemical cell [32]. This cell (shown in the Supplementary Material in the section concerning the *operando* study of BiSb by XAS), based on a previous one developed for *operando* XRD measurements [49], allows the investigation of electrode materials cycling under the same experimental conditions as those commonly employed in typical laboratory cells, thus enabling a simplified association of the *operando* XAS results to the lab-scale electrochemical tests. This cell was later also successfully adapted for *operando* Mössbauer [50], infrared [16] and Raman [19] spectroscopy, and even applied for simultaneous XRD-Mössbauer spectroscopy studies [51].

At ICGM, this cell was applied first to the relatively simple study of mixed metal phosphates with olivine structure with general formula $LiFe_xMn_{1-x}O_4$ as cathode materials for LIB [52]. In this case, the valence state of transition metal cations was deduced from the energy shift and the simultaneous change in the shape of the absorption edge. Quantitatively, both *operando* Fe and Mn K-edge XANES spectra of a sample with composition $LiFe_{0.33}Mn_{0.67}PO_4$ were fitted using a linear combination of the corresponding spectra of the pristine and of the fully lithiated material. The result of this procedure, shown in Fig. 1 allows decoupling the sequential oxidation of Fe and Mn in correspondence to the first and second potential plateau, respectively. Interestingly, an almost linear relationship between the amount of total metal (Mn and Fe together) in the trivalent state and the charge supplied to or released from the battery, is found showing that the main reactions of Li at the working potentials used in this test are indeed the oxidation and reduction of these two metals.

The same type of electrode material was also used in a second work as a benchmark for our first application of chemometric methods to data analysis, namely Principal Component Analysis (PCA) and Multivariate

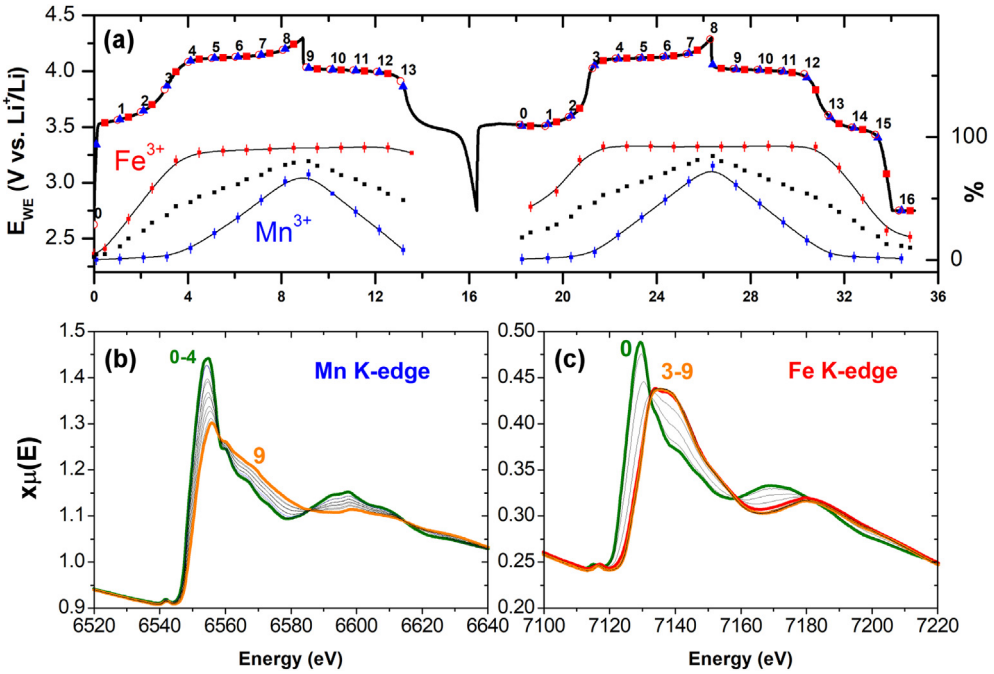

Fig. 1. (a) Quantitative evaluation (in % of each metal) of the Fe^{3+} and Mn^{3+} content during the first two charge/discharge cycles obtained from the linear combination fitting of the *operando* Mn (b) and Fe (c) K-edge XANES spectra of $LiFe_{0.33}Mn_{0.67}PO_4$ recorded upon cell operation at C/10 rate (a). Some spectra between the two cycles could not be recorded due to beam loss during cycling.

Curve Resolution - Alternating Least Squares (MCR-ALS) [53]. In fact, the combined use of PCA and MCR-ALS offers a unbiased separation method to process large sets of data by expressing them based on their similarities and differences.

In short, PCA is a factor analysis, *i.e.*, a multivariate technique for reducing matrices of data to their lowest dimensionality by the use of an orthogonal factor space: in such methods, the analyzed matrix corresponds to the experimental spectra, and each spectrum is considered as an n-dimensions vector with n corresponding to the number of points within each XAS spectrum. The first principal component has the largest initial variance, *i.e.*, alone it takes into account as much as possible the whole set of data. The following principal components are built orthogonal to the first one, and allow the reproduction of the experimental spectra with the highest possible variance via adapted linear combinations of them. This supposes that the group of analyzed spectra is intrinsically bilinear, which means that all spectra can be expressed as linear combinations of an orthogonal basis set of uncorrelated spectra. This basis set, which has a lower dimensionality than the number of original spectra, is thus obtained from the calculation. In the different linear combinations which are built to reconstruct each experimental spectrum, the multiplication factors of the principal components are usually called scores. The so-obtained principal components are only orthogonal mathematical functions and not real spectra, nevertheless their determination reveals the number of independent spectral components that can be used to describe the whole set of experimental data. Several methodologies are then available to reconstruct the corresponding real XAS components as well as their evolution, such as the MCR-ALS analysis tool. A detailed description of this method from a theoretical point of view is given by Tauler et al. [54,55] who also proposed this method for the analysis of *in situ* spectroscopic data. For more details about the application of these algorithms to *operando* XAS for catalysts or batteries, see Refs. [56–58].

In the case of Fe-Mn mixed-metal olivine cathodes, these methods were applied independently to both whole sets of *operando* Fe and Mn K-edge EXAFS spectra in order to extract the significant information on the evolution of the local electronic and structural properties of both metal centres during oxidation as a function of the Li content. This innovative approach enabled the detailed reconstruction of the whole reaction mechanism, revealing the simultaneous evolution of the structure of both metal centres even when they were not directly participating to the redox process [53]. In particular, the study of the evolution of the first coordination shell in the Mn K-edge EXAFS spectra, and more specifically its separation into two sub-shells with very different bond distances, allowed the precise description of the Jahn-Teller effect occurring upon oxidation of the manganese centres. This effect is known to be detrimental to the performance of such mixed-metal systems, partially hampering their complete delithiation.

Similar studies were also conducted on TiO_2-based insertion anode materials as high energy density alternative to commercially applied lithium titanate $Li_4Ti_5O_{12}$. *Operando* XAS was used to follow electronic and local structural changes upon lithiation of anatase and TiO_2(B) polymorph, which provided the typical spectra shown in Fig. 2. Even though both polymorphs are characterised by the same theoretical specific capacity of 336 mAh/g, corresponding to the insertion of 1 Li into the structure and the reduction of Ti^4+ to Ti^3+, only about 0.6 Li+ can be reversibly inserted into anatase (≈200 mAh/g). With TiO_2(B), conversely, higher reversible capacities exceeding ≈200 mAh/g can be reached [59]. Moreover, better rate capabilities are reached using TiO_2(B) using materials with similar particle size distributions. Indeed, these differences in performance are related to their different crystal structure implying distinct electrochemical reaction paths vs. lithium. In fact, the lithiation of anatase phase undergoes successive reaction steps: a first monophasic insertion is followed by a biphasic lattice transformation from a tetragonal to an orthorhombic structure, which is then retained during the following insertion which is accompanied by 4% lattice expansion [60]. XAS coupled to XRD showed that the first monophasic step, occurring up to ≈0.1 Li, does not inflict any local or global structural changes, whereas the following biphasic and monphasic reactions bring along a deformation of the octahedral coordination of Ti (detected, among other, from the modification of the XANES pre-edge features) and a gradual expansion of the coordination shells [61]. On the other hand, the insertion of Li^+ in TiO_2(B) follows a monophasic reaction path, with the crystal structure only subject to minor extensions upon lithiation (cf. Fig. 2) [62]. In the latter case, EXAFS was particularly

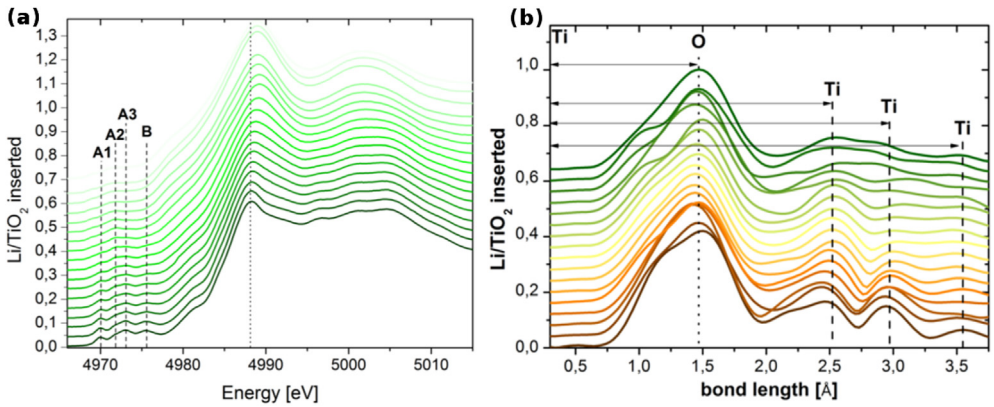

Fig. 2. XAS *operando* Ti K-edge spectra depicting the evolution of (a) XANES pre-edge and main edge feature of TiO_2 anatase and (b) phase-uncorrected EXAFS local structure of TiO_2(B) upon lithitation. A1, A2, A3 and B features of the XANES pre-edge of anatase and their evolution are highlighted in (a).

useful to show for the first time that the structural evolution upon lithiation of TiO_2(B) follows a two-regime process which matches the characteristic twin-peak of its electrochemical signature (not shown). These insights could hence be utilized to better understand the differences in mechanism and cycling performance of the two polymorphs [59,60].

In addition to these works, the use of *operando* XAS was extended to other electrode materials in the framework of collaborations with other institutes. For instance, in the last years a growing activity in the investigation of the electrochemical mechanism of Prussian Blue analogs was carried out in collaboration with the University of Bologna [63–66]. Among the main results of these studies, we can highlight a study on copper hexacyanoferrate performed simultaneously by Fe and Cu K-edge XAS, in which it was showed that both metals have a redox activity during lithiation [66], as well as a parallel work on Prussian Blue analogs where the cyanide groups are replaced by redox-active nitrosyl ligands, in which the redox activity is shared on three different centres, *i.e.*, the nitrosyl group and the two transition metals [64].

2.3. Studies carried out at ICGM: lithium-sulfur batteries

Simultaneously, a comprehensive work on Li-sulfur systems was also initiated in the framework of the European project EUROLIS. LSB are particularly interesting devices, since the combination of lithium and the inexpensive and naturally abundant sulfur in an electrochemical cell corresponds to the considerable theoretical energy density of 2600 Wh/kg. Even though the maximum practically accessible energy density is predicted to be at best 600 Wh/kg, it remains much higher than that of LIB [67,68]. In spite of these promising properties, LSB also suffer from several drawbacks: the main one is surely the diffusion of polysulfides (Li_2S_n), produced during the first steps of the reduction of sulfur and highly soluble in the electrolyte, which cause the well-known 'shuttle' phenomenon [69]. The second main drawback is the insulating nature of both solid Li_2S and elemental sulfur, which preclude the typical preparation of electrodes by casting formulated inks containing sulfur and carbon additive(s) on aluminum current collectors [70,71]. All these disadvantages are strongly impacting both capacity and cyclability of LSB, causing rapid fading and low coulombic efficiency.

Several improvements have been suggested to tackle these drawbacks, including the confinement of sulfur into porous conductive carbon materials to reduce its mobility and improve the electronic conductivity, or the preparation of multifunctional positive electrodes, enhancing sulfur loading and promoting the interaction of polysulfides with the electrode host to prevent their diffusion in the electrolyte [72–76]. In many studies, XAS was employed among other techniques for the detailed investigation of the electrochemical mechanism and the diffusion (or retention) of polysulfides, as well as of possible failure paths [77]. In our works, we mostly employed sulfur K-edge XANES to obtain semi-quantitative information about the evolution of the relative amounts of the different sulfur species during the discharge and the charge process, as well as about the modification of the total concentration of sulfur in both cathode and electrolyte, which is connected to the diffusion of the polysulfides in the whole battery [78–82]. This was performed mainly by fitting the XANES spectra, measured either at the electrode surface or on the separator soaked with the electrolyte, to linear combinations of reference spectra of pure sulfur, polysulfides and Li_2S. Given the low energy of sulfur K-edge (only 2.47 keV), these experiments had to be performed in fluorescence mode on a modified version of our *in situ* cell, equipped with an extremely thin beryllium window (8 μm) and kept inside a tight container under pure He flow, specifically designed by the beamline team at the XAFS beamline of synchrotron Elettra (Trieste, Italy) [79,80].

In a particularly experiment, in addition to the XANES data, also EXAFS spectra could be employed for the study the electrochemical mechanism [79]. Such study, in fact, was carried on using a sulfur-free electrolyte salt based on the LiTDI (Lithium 4,5-dicyano-2-(trifluoromethyl)imidazole) salt dissolved in a 1:1 mixture of tetraethylene glycol dimethyl ether (TEGDME) and dioxolane (DOL), which thus allowed following the EXAFS contribution of the evolving sulfur species during cycling, usually masked by the dominant sulfonate-based electrolyte salt signal. The fitting of the EXAFS spectra during the discharge provided the fraction of Li_2S in the electrode as well as the average coordination number of the sulfur centres in sulfur and polysulfides (cf. Fig. 3). From the average number of neighbours in the sulfur chains it was possible to determine the average length of the polysulfide chains (dashed lines in Fig. 3) formed in the electrode during cycling. This results allowed us to thoroughly describe the discharge mechanism in Li-sulfur systems: the pristine S8 is first converted into $S8_{2-}$ along the plateau at high potential; $S8_{2-}$ is then transformed into shorter polysulfides during the potential slope, and finally Li_2S gradually precipitates during the low potential plateau. This mechanism could be later confirmed by other techniques, such as for instance Raman spectroscopy [19].

2.4. Studies carried out at ICGM: conversion anode materials for LIB

At the negative electrode side, the application of *operando* XAS to the study of materials undergoing the conversion reaction such as $NiSb_2$ and TiSnSb provided valuable insights on the activity and role of the different elements in the complex electrochemical conversion mechanism. In a conversion reaction [9], lithium reacts with a binary compound containing a transition metal (M = Ti, Mn, Fe, Co, Ni, etc.) and a *p*-group element (X = O, P, Sb, Sn, etc.), according to:

$$M_aX_b + (b^*n)Li = M + b\ Li_nX \quad (1)$$

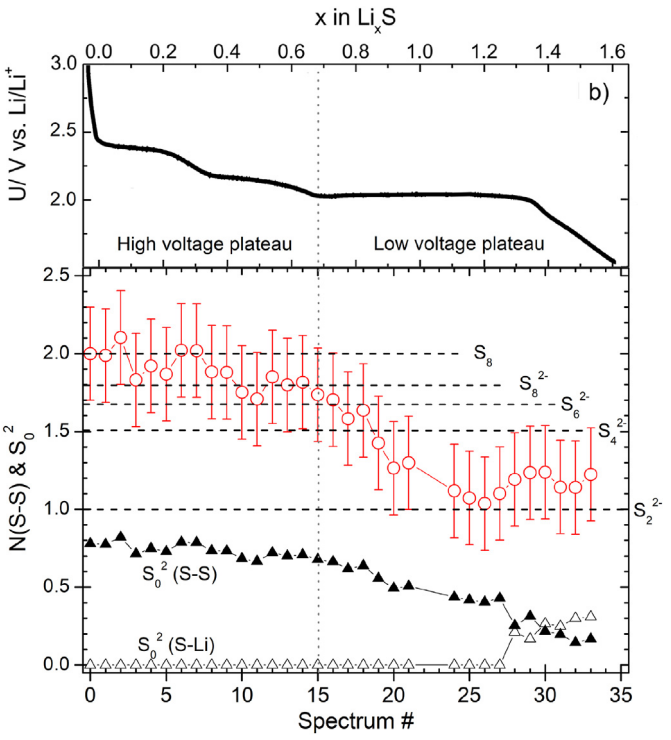

Fig. 3. Average coordination number of S in sulfur and polysulfides (red circles) during the first discharge determined from the EXAFS spectra measured in the 1 M LiTDI TEGDME:DOL electrolyte, and corresponding amplitude attenuation factor S_0^2 of the Li-S and S-S contributions, indicating the growth in intensity of Li_2S and the decrease of polysulfide contribution towards the end of the discharge. The average coordination of the most important polysulfides is represented by the horizontal dashed lines. The corresponding electrochemical curve measured during the discharge is shown on top. (For interpretation of the references to colour in this figure legend, the reader is referred to the Web version of this article.)

First verified for transition metal oxides, conversion reactions are rather common also for other chalcogenides, pnictogenides and carbon group semimetals. Conversion materials, *i.e.*, materials undergoing the conversion reaction, allow reversible capacities as high as 1500 mAh/g, far exceeding that of graphite (372 mAh/g), the negative electrode material commonly used in commercial Li-ion batteries. During a conversion reactions, the pristine electrode material loses its crystallinity, and composite materials including nanosized species are formed, making it impossible to follow the reaction by long-range order techniques such as XRD. Moreover, the species formed at the end of the discharge process are particularly reactive and unstable, and therefore the use of *operando* techniques becomes essential for the study of reaction mechanisms.

Among conversion materials, pnictogenides with general formula M_xSb_y are expected to react with lithium by forming a matrix of Li_3Sb in which nanoparticles of the transition metal M are embedded. The actual reaction mechanisms, however, is usually more complex and dependent on the specific compound. For instance, $FeSb_2$ [83], is known to form intermediate lithiated insertion phases before starting the veritable conversion reaction, and additional phases might also form throughout the whole electrochemical cycle.

Also $NiSb_2$ undergoes a relatively complex lithiation process to form nickel metal and Li_3Sb for a theoretical capacity of 532 mAh/g [84]. However, while XRD suggested the possible formation of an intermediate ternary insertion solid solution during the first discharge, it did not allow following the whole mechanism due to the complete amorphisation of the system. With the help of *operando* Ni K-edge XAS, on the other hand, it was possible to follow the chemical state of Ni during the first two lithiation/delithiation cycles, showing that a reversible conversion takes place, with the formation of Ni metal nanoparticles at the end of lithiation and the reversible formation of a Ni-Sb phase close to pristine $NiSb_2$ at the end of the delithiation process [85]. Moreover, strong differences were observed when comparing *operando* results with *ex situ* measurements on cycled $NiSb_2$ at the same state of charge prepared two weeks before the XAS measurement campaign. Indeed, these systems were found to produce metastable species during the discharge which undergo relaxation under OCV conditions, and which are thus detrimental for a possible effective application of such materials in commercial systems. In short, this comparison highlighted the importance of real-time investigation tools for the study of battery materials, and particularly for those undergoing a conversion reactions or containing particularly reactive species.

More recently, *operando* XAS was applied to the study of the electrochemical cycling mechanism of the ternary intermetallic TiSnSb [86], a promising conversion-type negative electrode material for lithium batteries [87,88]. However, differently from the case of $NiSb_2$, this study was carried out at three different absorption edges, namely Ti, Sn, and Sb K-edge, and data analysis was performed by using chemometric tools such as PCA and MCR-ALS in order to extract the maximum information contained in the whole set of *operando* data. Given the very large difference in energy between the K-edges of Ti and of the other two *p*-group elements, implying very different sample thicknesses, as well as beamline settings (monochromator, detectors, etc.), two different experiment had to be performed: a first experiment at the Ti K-edge revealed that the direct conversion of TiSnSb upon lithiation leads to the formation of Ti metal nanoparticles. The latter were identified from the modification of the XANES spectra, which become very similar to that of Ti metal, and especially by the loss of Sb and Sn neighbours around the Ti centres, and the simultaneous increase of the number of the Ti ones. EXAFS also confirmed that this reaction is reversible upon the following delithiation, with Ti binding back to both Sn and Sb, finally confirming that TiSnSb reacts with lithium through an authentic conversion reaction [86]. The second experiment carried out simultaneously at both Sn and Sb K-edges confirmed that both elements are electrochemically active upon lithiation. In fact, EXAFS detected a drastic modification in nature, bond distance and number of neighbours around both Sn and Sb centres, substantiating the formation of Li_7Sn_2 and Li_3Sb previously detected by ^{119}*Sn* Mössbauer spectroscopy and XRD [87]. Globally, small but significant differences between the EXAFS spectrum of the material obtained after one complete electrochemical cycle and that of pristine crystalline TiSnSb suggest the formation of a ternary "Ti–Sn–Sb-like" species with distinct structural properties from pristine TiSnSb.

Data analysis was performed using a chemometric approach, which enabled us to visualize for the first time that the lithiation and delithiation reactions of Sn and Sb do not occur simultaneously, but are slightly shifted. In fact, as depicted in Fig. 4, during charge, when the lithiated species are oxidized one can observe that the onset of Sn EOC component formation (red curve) precedes the Sb one (blue curve), thus confirming that the two metals do not react at the same time, in spite of a certain overlap between their respective reaction. In this way, it was possible to attribute the presence of two plateaus in the electrochemical signature, represented by the two peaks in the inverse of the derivative of the potential with the charge at ≈ 0.5 and ≈ 0.9 V in Fig. 4, to this shift in the reaction of the two *p*-group metals. This result highlights the advantage of using a chemometric approach, with respect to state-of-the-art conventional ones, in solving a complex mixture reaction processes and reliably reconstructing them [57].

2.5. Studies carried out at ICGM: Sb-based anode materials for NIB

In one of our first studies on NIB in 2012, we demonstrated for the first time that pure antimony can be successfully used as anode material, sustaining a capacity close to 600 mAh/g with excellent cycle life and rate capability [89]. This result showed that, contrary to LIB, antimony has a very specific affinity for sodium, and gave a strong impulse to our

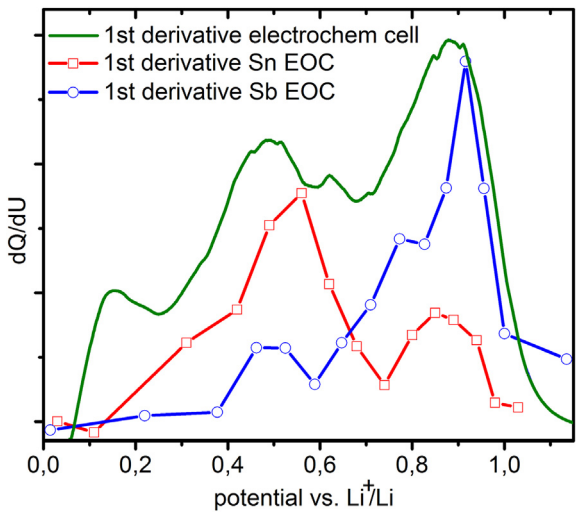

Fig. 4. Derivatives of the MCR-ALS concentration profiles of the Sn (red) and Sb (blue) EOC components and overall dQ/dV profile measured in the *operando* cell (green) during charge. (For interpretation of the references to colour in this figure legend, the reader is referred to the Web version of this article.)

research which was thus extended to many other Sb-based negative electrode materials such as SnSb [90] and $FeSb_2$ [91]. The specific affinity of Sb for Na in all these compounds is strongly dependent upon the electrochemical reaction mechanism, which does not simply go through the formation of the intermediate species expected from the phase diagram as in the case of LIB, but rather through unexpected amorphous phases not visible by XRD, and which could be identified, in the case of pure Sb, only by a complex approach involving *operando* Pair Distribution Function (PDF) analysis, *ex situ* nuclear magnetic resonance (NMR) spectroscopy and the support of Density Functional Theory (DFT) calculations [92].

In the framework of this large research project, XAS was also applied with alternate success for the comprehension of the electrochemical reaction mechanisms of the different materials. In the case of pure Sb, for instance, a study by *operando* Sb K-edge XAS assisted by a chemometric approach, ^{121}Sb Mössbauer spectroscopy and DFT calculations confirmed that Sb reacts with Na to form disordered Na_3Sb via the formation of amorphous Sb as an intermediate and that, upon charge, Na_3Sb is gradually desodiated to amorphous Sb [48]. However, it was possible to demonstrate that XAS (as well as Mössbauer spectroscopy) are intrinsically unable to spot the other intermediate Na_xSb phases previously identified by NMR and PDF [92].

Differently from the example of Sb, XAS was very useful in the study of the cycling mechanisms of both SnSb and $FeSb_2$, which also go through extensive amorphisation during cycling. In the case of SnSb, its reversible sodiation-desodiation reaction was investigated by simultaneous *operando* Sn and Sb K-edge XAS and ^{119}Sn Mössbauer spectroscopy assisted chemometric data analysis [31]. During the sodiation, which goes through a two-step process, it was not only possible to disclose the formation of Na_3Sb and $Na_{15}Sn_4$, a rarely observed phase in pure Sn-based electrodes, at the end of the discharge, but also to identify for the first time an amorphous form of α-Sn, thermodynamically unstable at ambient conditions, as a reaction intermediate, see Fig. 5. These insights on the mechanism of SnSb vs. Na provide a basis for understanding its excellent cycle life and capacity retention, which lies in the gradual formation of amorphous, nano-confined intermediate phases and correlated elastic

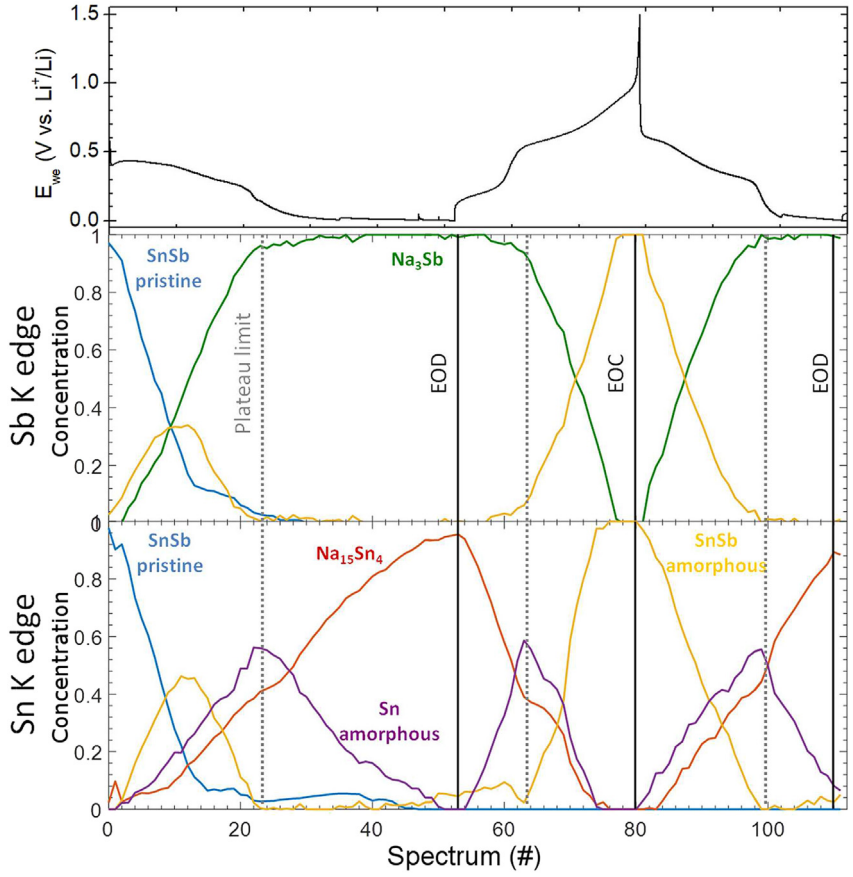

Fig. 5. Evolution of the concentration of the MCR-ALS spectral components for Sn and Sb K-edges during subsequent sodiation, desodiation and sodiation of SnSb, and corresponding experimental electrochemical signature. EOD and EOC mean the end of discharge and end of charge, respectively.

softening of highly sodiated tin and antimony phases which have enhanced ability to absorb and mitigate the strong volume changes occurring upon sodiation and desodiation.

In the case of $FeSb_2$, the combination of *operando* Sb K-edge XAS, magnetic measurements and ^{57}Fe Synchrotron Mössbauer Spectroscopy, the latter used for the first time in the field of energy storage materials, allowed us to clarify the role of iron and antimony in the reversible sodiation mechanism [93]. Our findings show that the reaction of Na with $FeSb_2$ during discharge leads to the formation of Na_3Sb along with superparamagnetic Fe nanoparticles containing small fractions of Sb, as previously detected by low temperature *ex situ* ^{57}Fe Mössbauer spectroscopy [91]. Pristine $FeSb_2$ is never recovered by desodiation, while iron nanoparticles grow in size, and continue growing also along the following discharge, as testified by the increase of the Lamb-Mössbauer factor of the spectral component representing Fe nanoparticles. Even though such nanoparticles remain electrochemically inactive, they play a active role in the reduction and stabilization of the polarization as well as in the reversibility of the electrochemical sodiation of antimony.

Along with these studies, other Sb-containing electrode materials were investigated and showed interesting performance. Among them, one has to consider the case of Bi-Sb system, which has recently shown interesting properties as anode material in K-ion batteries (KIB) and Mg-ion batteries (MIB) [94,95]. In the following section, the study of its electrochemical mechanism by several complementary techniques including XAS will be presented and discussed in detail. This work will highlight both the ability of XAS in providing useful information on electrochemical mechanisms, and the advanced technology of the ROCK beamline at Synchrotron Soleil allowing the simultaneous *operando* investigation of several elements presenting absorption edges at very different energies in battery materials.

3. An experimentally challenging case study: the sodiation of $Bi_{0.50}Sb_{0.50}$ simultaneously followed by *operando* Sb K-edge and Bi L_3-edge XAS

3.1. Introduction

Both antimony and bismuth, elements of the group V, crystallise in the rhombohedral space group [PDF 01-085-1329 and PDF 01-085-1322, respectively] [96,97], and form a solid solution over the whole composition range [98]. Bi-Sb alloys have been studied in the past for their peculiar properties. While pure bismuth and antimony show a relatively good electric conductivity, their alloys show complex semiconductor properties strongly dependent upon the composition, and some of them, *e.g.* $Bi_{0.9}Sb_{0.1}$, were the first experimentally observed 3D topological insulators, *i.e.*, materials with conducting surface states and an insulating interior [99]. Bi-Sb alloys also showed superconductivity properties: for instance $Bi_{0.4}Sb_{0.6}$ is a superconductor with a critical temperature T_c, of approximately 2 K [100]. Lin et al., on the other hand, reported the thermoelectric properties of $Bi_{1-x}Sb_x$ alloy nanowires [101]. In the last decade, several examples of application of Bi-Sb alloys as anode materials in battery systems were published, including LIB, NIB and MIB.

For instance, Li et al. recently reviewed the works concerning the application of Bi and Sb in NIB, underlining in particular the potential of Bi-based materials in batteries owing to their multiple features such as narrow band gap, ion conductivity, and environmental friendliness, and indicating a few examples of Bi-Sb alloy systems [102]. Zhao et al. studied Bi-Sb alloys prepared by high energy ball milling, finding that such alloys exhibit electrochemical performances in NIB superior to those of their counterparts Bi and Sb [103]. The same materials also show elevated capacities in LIB at high current rates. Xie et al. proposed a ternary Sn-Bi-Sb system for NIB, describing a clear relationship between the cycling properties and the composition [104]. The formation of ternary Na-Bi-Sb alloys has been suggested as the basis for the good cycling stability. Arthur et al. used electrodeposited $Bi_{1-x}Sb_x$ as anodes for Mg-ion batteries [105]. In this system, the best cycling properties over 100 cycles were obtained with $Bi_{0.88}Sb_{0.12}$ and Bi, while Sb failed to show appreciable capacity. More recently, Murgia et al. showed that in Mg-ion system Sb alone is not active, and that only the association of Sb with Bi enables the electrochemical magnesiation of Sb, leading to the formation of monophasic $Mg_3(Sb_{1-x}Bi_x)_2$ alloy, identified by solid state NMR, at the end of the discharge [94]. This last paper is the only one, to the best of our knowledge, where some specific insights concerning the cycling mechanism of Bi-Sb alloys vs. alkali and alkaline-earth metals could be proposed with the support of diffraction and/or spectroscopy techniques.

In this section, the electrochemical sodiation mechanism of $Bi_{1-x}Sb_x$ alloys is investigated by a combination of XRD, XAS and ^{121}Sb Mössbauer spectroscopy. Several polycrystalline $Bi_{1-x}Sb_x$ compositions (with $x = 0.5$, 0.56, 0.78 and 0.9) were synthesized by high energy ball milling, and characterised by XRD. Their electrochemical properties were studied in half cells vs. Na metal using a 1 M $NaClO_4$ in PC electrolyte containing 5% fluoroethylene carbonate as additive. The detailed results of this study are reported in the Supplementary Material. In short, a strong dependence of the capacity on composition is observed, with a decrease of the capacity retention with the decrease of the Sb content. The full *operando* characterisation by XRD as well as by simultaneous Sb K-edge and Bi L_3-edge XAS is presented for the composition $Bi_{0.5}Sb_{0.5}$. More details about the synthesis of the materials and of the electrodes, as well as about the different characterisation techniques, are given in the Supplementary Material.

3.2. Characterisation of pristine Bi-Sb alloys

The $Bi_{1-x}Sb_x$ alloys with $x = 0.5$, 0.55, 0.80 and 0.9 prepared by ball milling were analyzed by XRD as shown in Fig. 6. All $Bi_{1-x}Sb_x$ samples crystallise as expected in the same $R\bar{3}m$ space group. The diffraction patterns clearly show the shift of the (012) diffraction peak to higher angles with the increase of Sb ratio in the alloys. The same trend is observed for the other diffraction peaks (cf. Supplementary Materials).

The results of profile matching of the diffraction patterns of the $Bi_{1-x}Sb_x$ samples are reported on Table 1, the rhombohedral Bi-Sb structure being expressed in terms of equivalent hexagonal unit cell. The corresponding refined *a* and *c* hexagonal cell parameters and volume decrease with increasing Sb content, in line with the size of the atomic radii of Sb and Bi (1.45 and 1.60 Å, respectively). The composition of $Bi_{1-x}Sb_x$ samples were confirmed from the calculation of the *a* lattice parameter using Berger's formula [106]:

$$a = (0.454469 \pm 0.00044) - (0.02398 \pm 0.00072)x \quad (2)$$

As shown in Fig. 7, the observed linear variation of the lattice parameters *a* and *c* with Sb concentration for $Bi_{1-x}Sb_x$ samples clearly reveals that they follow the Vegard's law. The sample used for the *operando* XRD and XAS study is $Bi_{0.50}Sb_{0.50}$, characterised by a 0.50/0.50 Bi/Sb atomic ratio as confirmed by XRD (cf. Fig. 7), and hereafter simply labelled *BiSb*.

Additional analyses by ^{121}Sb Mössbauer spectroscopy (cf. Supplementary Material) did not provide further information, this technique not being able to discriminate the different compositions.

3.3. The reversible sodiation of BiSb followed by operando XRD

The *operando* XRD patterns collected through the whole first discharge/charge cycle and the following second discharge of a *BiSb* electrode are shown in Fig. 8. The whole series of data can be divided in three parts: the first discharge, the first charge and the second discharge. The details of the different phases identified during cycling are resumed in the Supplementary Materials.

The first XRD pattern corresponds to the pristine *BiSb*, and the peak at 48° (2θ) comes from the beryllium window of the *in situ* cell. After the insertion of 1 Na^+, most probably irreversibly consumed in the degradation of the electrolyte leading to the formation of the solid electrolyte

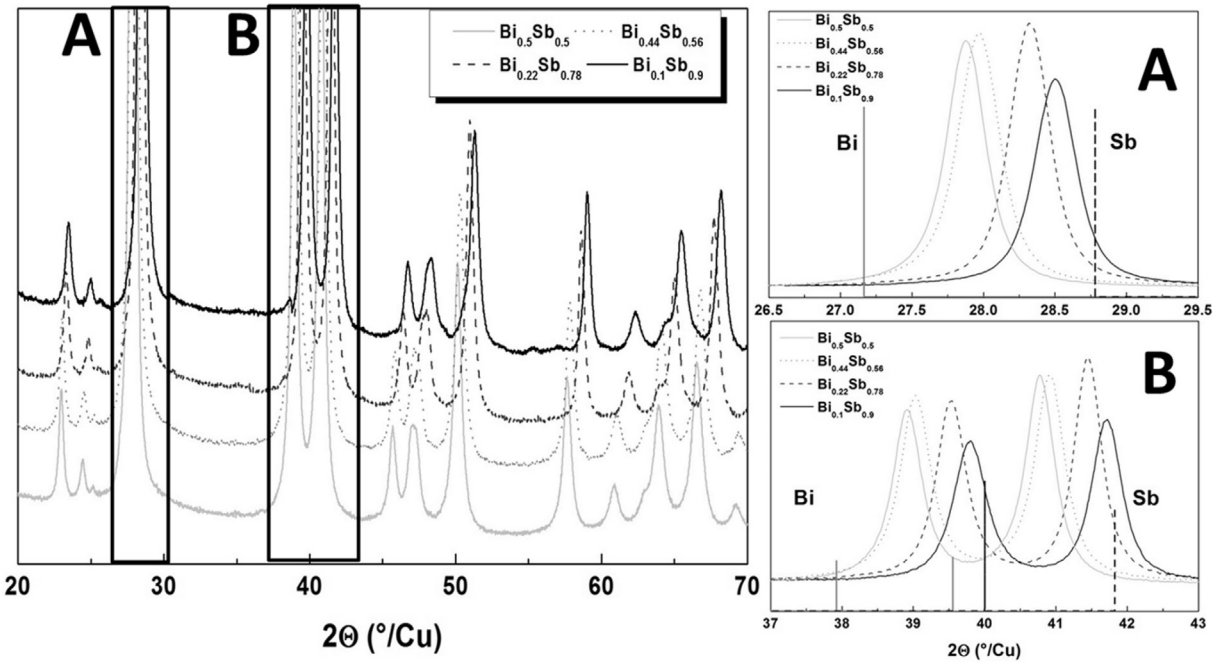

Fig. 6. a) XRD patterns of $Bi_{1-x}Sb_x$ alloys with x = 0.9, 0.78, 0.56, 0.5 (top to bottom); b) Evolution of the (012) diffraction profile for different concentrations of Sb; the position of the profiles of pure Sb and Bi (vertical lines) are presented for comparison.

Table 1
Lattice parameters resulting from the refinement of the XRD patterns of the $Bi_{1-x}Sb_x$ samples. Unit cell parameters of Sb and Bi are given for comparison, standard deviations are given in brackets.

Compound	*a*, Å	*c*, Å	*α*, *β*, *γ*, Å	*V*, Å^3
Sb	4.3070(1)	11.2730(2)	90, 90, 120	181.10(1)
$Bi_{0.10}Sb_{0.90}$	4.328(1)	11.357(1)	90, 90, 120	184.27(1)
$Bi_{0.22}Sb_{0.78}$	4.355(1)	11.434(1)	90, 90, 120	187.81(1)
$Bi_{0.44}Sb_{0.56}$	4.410(1)	11.576(1)	90, 90, 120	194.98(1)
$Bi_{0.50}Sb_{0.50}$	4.423(1)	11.605(1)	90, 90, 120	196.66(1)
Bi	4.536(1)	11.850(1)	90, 90, 120	211.15(1)

interphase (SEI), *BiSb* starts being consumed while a new phase, isostructural to both Bi and Sb ($R\bar{3}m$), emerges and reaches its maximum intensity at the end of the process. Its refined cell parameters are in between those of Na_3Bi and Na_3Sb ($P63/mmc$ hexagonal space group). During the following charge, this new phase with a composition close to $Na_3(Bi_{0.50}Sb_{0.50})$ is progressively consumed leaving its place to a new set of peaks which can be attributed to a phase close to NaBi [PDF 00-004-0701], but with slightly lower *a* and *c* cell parameters. This difference in cell parameters could be due to the substitution of a portion of Bi by Sb, leading to a ternary compound with composition $NaBi_{1-x}Sb_x$. It is worth noticing that it coincides with the appearance of a peak at about 0.64 V in the derivative of the galvanostatic curve (cf. Supplementary Materials). At the end of the charge, the ternary intermediate $NaBi_{1-x}Sb_x$ has completely disappeared in favor of a Bi-Sb alloy isostructural to both Bi and Sb ($R\bar{3}m$) with refined cell parameters indicating a composition close to $Bi_{0.9}Sb_{0.1}$ according to Vegard's law (cf. Fig. 7). Considering the Sb-poor stoichiometry of this binary phase, amorphous antimony is also expected to be simultaneously formed, as previously observed for the desodiation of sodiated Sb electrodes [48,89,92]

During the second discharge, the Bi-Sb alloy formed at the end of the charge disappears progressively in favor of the formation of the ternary $NaBi_{1-\delta}Sb_\delta$ intermediate, already identified during the first charge, before leading to the final ternary $Na_3(Bi_{0.5}Sb_{0.5})$ analogous to the end of the first discharge, which demonstrates a complete and quite reversible sodiation/desodiation mechanism. It is worth noting that the combination of Sb and Bi helps to this reversibility compared to pure Bi. On the other hand, the presence of Bi enables the formation of crystalline intermediate phases, differently from the case of pure Sb where the intermediate sodiated species were fully amorphous.

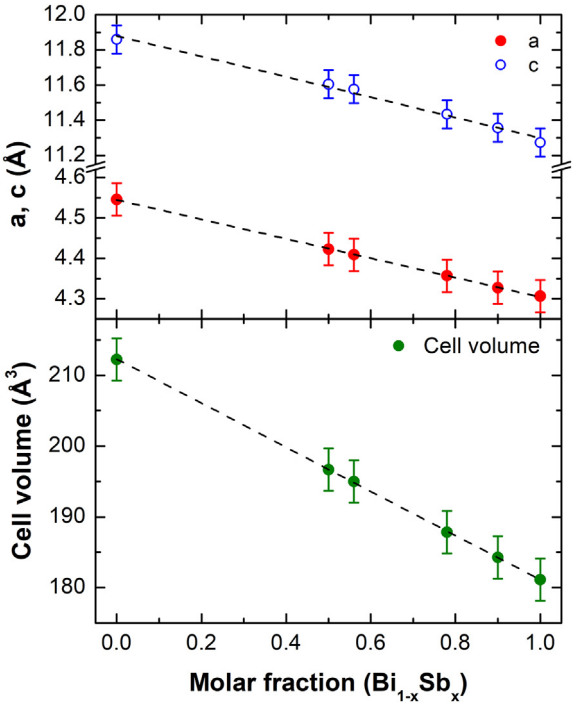

Fig. 7. The variation of lattice parameters *a* and *c* (top) and that of the unit cell volume (bottom) versus the molar fraction x of antimony in $Bi_{1-x}Sb_x$ alloys. The dashed lines should be considered as guides to the eye.

3.4. The reversible sodiation of BiSb followed by operando Sb K-edge and Bi L_3-edge XAS

The *operando* Sb K-edge and Bi L_3-edge XAS study was performed on

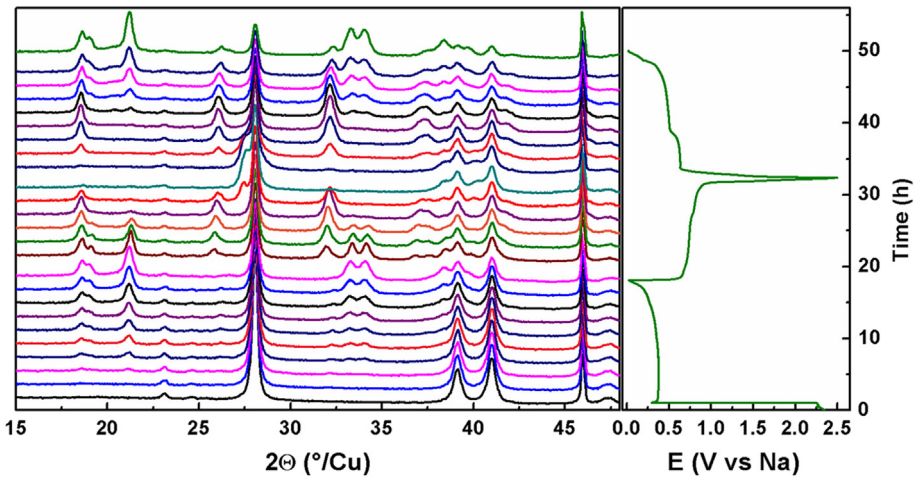

Fig. 8. *Operando* XRD patterns collected at various stages of discharge and charge of *BiSb* (left) and the corresponding voltage profile (right).

the same sample used for the XRD study, labelled *BiSb*, at the beamline ROCK of Synchrotron Soleil (Gif-sur-Yvette, France). This measurement implies continuous alternate measurements of the XAS spectra of two elements with absorption edges at very different energies (Sb K-edge and Bi L_3 -edge are at 30491 and 13418 eV, respectively), and ROCK is, to the best of our knowledge the only beamline allowing such type of experiment [34]. The beamline is equipped with a first focusing mirror, the set of two rapidly interchangeable Quick-XAS Si(111) and Si(200) channel-cut monochromators covering a range of energies from 4 to 40 keV, each one coupled to an adapted set of mirrors used to eliminate the high order harmonics with a rejection coefficient ranging from 10^4 to 10^8 depending on the cut-off energy, and two sets of three ionisation chamber detectors rapidly exchangeable via a pneumatic system. This set-up allows the use of a wide range of sample environments which can be mounted on the motorized sample stage, and in particular the setting up of several *in situ* electrochemical cells which can be studied in parallel via a completely automatised system (cf. Supplemetanry Material). The flux available on the sample permits the measurement of XAS spectra with an acceptable signal-to-noise ratio if the studied sample is prepared with an adapted thickness (*e.g.*, a sample with a loading of 19 mg/cm^2 with a composition $Bi_{0.50}Sb_{0.50}$ will have an acceptable transmission at both edges, providing an absorbance step of 0.3 and 1.0 for the Sb K-edge and Bi L_3 -edge, respectively). The sample stage of the experimental set-up is shown in the Supplementary Material.

3.4.1. Bi L_3-edge XAS results

The *operando* Bi L_3-edge XAS spectra (XANES and EXAFS portions) collected during the first cycle (sodiation/desodiation) are shown in Fig. 9 (cf. Supplementary Material for the corresponding electrochemical cycling curve.) The absorption edge is characterised by large and broad features, and its overall shape and position varies only slightly during cycling. This result is somehow expected, the pristine and the formed compounds being all intermetallics. Consequently, the XANES part of the spectrum bears only negligible information and is hence of little use for the identification of the different species formed during the electrochemical process. On the other hand, the oscillation of the EXAFS part are rather intense and visible up to $k = 10$ Å^{-1}, and can thus be used to describe the average coordination around the Bi centres.

PCA was performed on the whole set of the XAS data in order to extract the maximum amount of useful information contained in the *operando* spectra. Since the XANES part is varying very little during the process, the differences between the principal components are concentrated in the EXAFS region. The variance plot obtained (cf. Supplementary Material) shows rather clearly that more than 98% of the variance of the XAS spectra can be described by three principal components, the

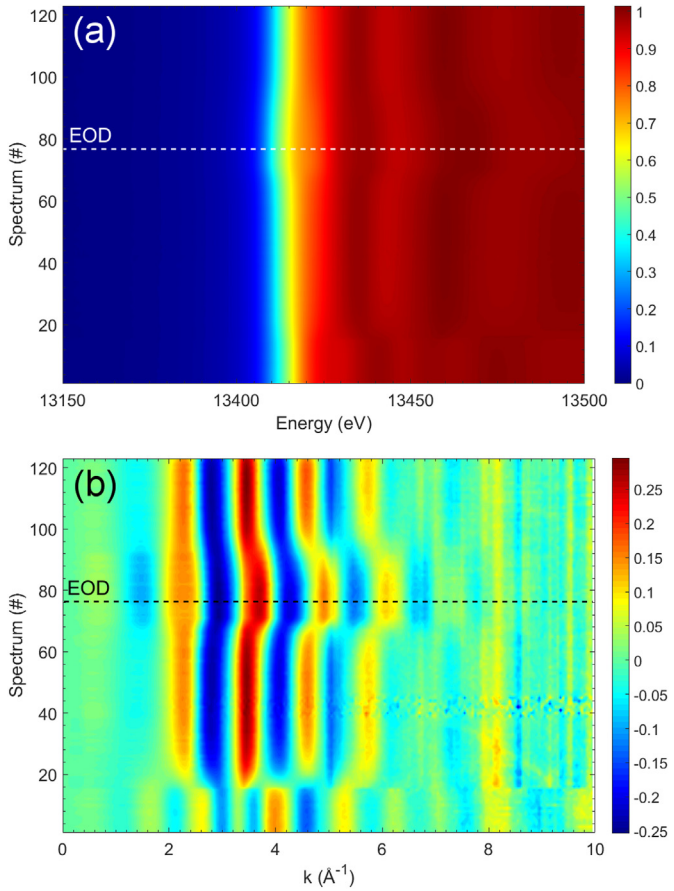

Fig. 9. (a) XANES and (b) EXAFS *operando* Bi L_3-edge XAS spectra measured during the first electrochemical cycles of *BiSb* electrode *vs.* Na. The horizontal line labelled EOD represents the end of the first discharge.

residual part can be attributed to the experimental noise. The examination of the shape of the principal components and of the respective scores (see details in the Supplementary Material) support this hypothesis, with both shape and evolution of the first three components varying gradually through the different processes, and those of the following ones changing in a totally hectic way.

Given that the so-obtained principal components are orthogonal mathematical functions and not real EXAFS spectra, it is possible, based

on their number, to reconstruct corresponding real EXAFS components as well as their evolution using the MCR-ALS method, recently reviewed in Ref. [57]. In this case, the MCR-ALS analysis produces the three EXAFS spectra shown in Fig. 10 together with their evolution along the electrochemical cycle. These components correspond perfectly to specific spectra measured along the *in situ* measurements, in line with their observed evolution (cf. Supplementary Material).

The obtained MCR-ALS components can thus be treated as normal spectra, and fitted using the conventional approach (cf. Supplementary Material for the details of the fits). Component 1 is satisfactorily fitted starting from the crystal structure of the Bi-Sb alloys, using three Bi-Bi and three Bi-Sb shells, confirming the homogeneous nature of the *BiSb*. The slightly elevated Debye-Waller factors obtained through the fit, however, indicate a certain degree of local disorder in the material.

Concerning component 3, which represents the fully sodiated electrode, only the first neighbour shell is visible, and can be relatively simply fitted with two sub-shells of Na nearest neighbours with rather large Debye-Waller factors. On the basis of these data, given the lack of information about the second neighbour shell, it is impossible to differentiate the possible formation of a ternary $Na_3(Bi_{1-x}Sb_x)$ alloy from that of simple Na_3Bi.

Finally, component 2 is fitted with three contributions including Bi, Na and Sb neighbours. All fitting attempts with only Na or with Na and Bi neighbours where unsuccessful. An optimisation of the number of Bi and Sb nearest neighbours, provided a composition close to the ternary $Na(Bi_{1-x}Sb_x)$ alloy, having the same crystal structure of NaBi. It is interesting to notice that this structure already forms at an early stage of sodiation before gradually disappearing when component 3 grows toward the end of the discharge.

3.4.2. Sb K-edge XAS results

The same data analysis approach was used also to study the *operando* Sb K-edge XAS spectra collected during the first cycle (cf. Supplementary Material). Differently from the Bi L_3-edge spectra, PCA analysis suggests the presence of four independent components, which where reconstructed using MCR-ALS, and that are shown in Fig. 11 together with their evolution along the electrochemical cycle. Only some of these components correspond to specific spectra measured along the *in situ* measurements, in line with their observed evolution (cf. Supplementary Material).

The fit of MCR-ALS components 1 and 3 is relatively straightforward, the two of them representing pristine $(Bi_{0.50}Sb_{0.50})$ and the material obtained at the end of discharge, $Na_3(Bi_{0.50}Sb_{0.50})$. Indeed, component 1 can be fitted with the same shells and virtually the same parameters used for fitting the corresponding Bi L_3-edge spectrum, whereas only the first Na shell of component 3 is visible in the spectrum, thus hampering the identification of its composition as in the case of the Bi measurement.

The other two components are more interesting, since they do not correspond to any experimental spectrum, and never reach a 100% intensity during cycling. Component 2 is very similar to component 2 found in the Bi L_3-edge data, and must be fitted including the contributions of Bi, Na and Sb neighbours. All other fitting attempts with fewer

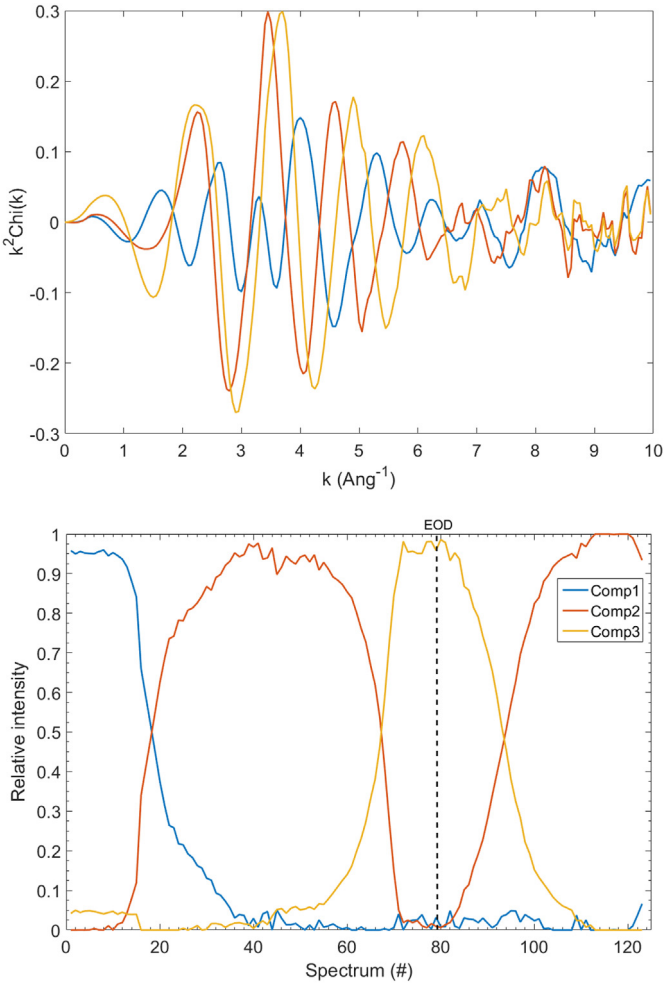

Fig. 10. EXAFS spectral components (top) obtained by MCR-ALS analysis of the *operando* Bi L_3-edge XAS spectra, and variation of their intensity (b) during electrochemical cycling. The vertical black line represent the end of the first discharge (EOD).

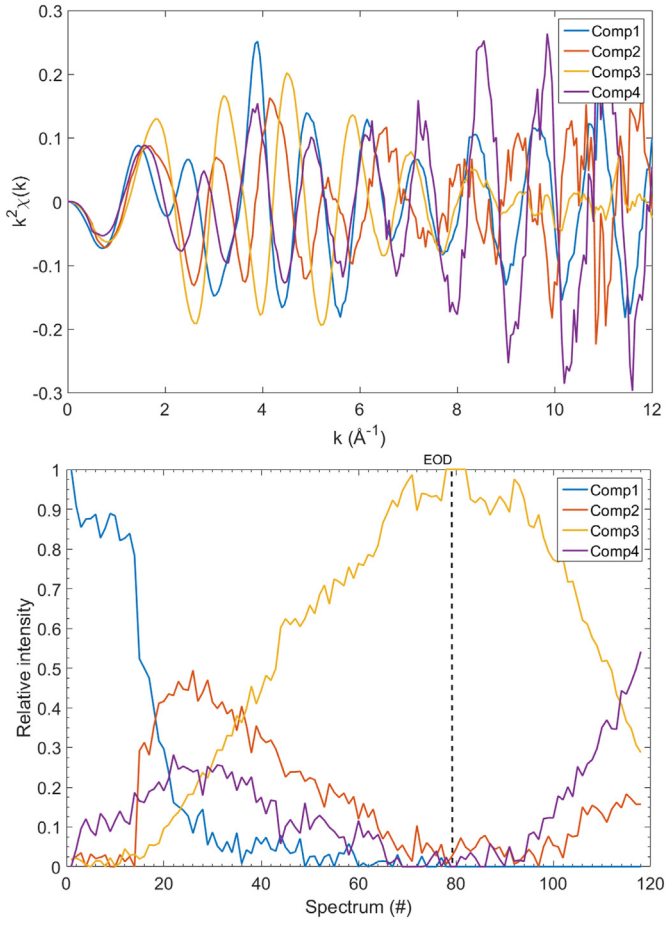

Fig. 11. EXAFS spectral components (top) obtained by MCR-ALS analysis of the *operando* Sb K-edge XAS spectra, and variation of their intensity (b) during electrochemical cycling. The vertical black line represent the end of the first discharge (EOD).

components were unsuccessful. As in the previous case, this component fits well with the composition of the ternary $Na(Bi_{1-x}Sb_x)$ alloy, having the same crystal structure of NaBi.

Component 4, instead, must be fitted with the two shells representing Sb and Na, whereas it does not contain any contribution from bismuth. Given the relative intensity of the two Sb and Na contributions, it fits well with the stoichiometry of NaSb, even though in a previous work we have demonstrated that the same signal can be obtained by a linear combination of the signals of amorphous Sb and Na_3Sb [48]. In any case, it belongs to chemical species not containing any bismuth, most probably amorphous in nature as observed for the pure Sb system.

3.5. Discussion

The electrochemical study of the different compositions (cf. Supplementary Material) shows a gradual modification of the cycling properties and of the mechanism on going from Sb to Bi, with a gradual decrease of the capacity retention and a corresponding gradual modification of the mechanism with the Bi content. In particular, the modification of the potential of the different plateaus with respect to those of pure Bi and Sb suggests the formation of different sodiated compounds, *i.e.*, the formation of ternary Na-Bi-Sb alloys both as intermediates during the discharge and as the final product obtained at the end of the discharge. This hypothesis is supported by *operando* XRD, which rather clearly confirms the formation of a compound with a composition close to $Na_3(Bi_{0.50}Sb_{0.50})$ at the end of the first discharge. EXAFS, on the other hand, is rather neutral to this conclusion, confirming the complete sodiation of both Bi and Sb but not providing any information about the second neighbours, *i.e.*, about the composition of the sodiated alloy. Unfortunately, also *ex situ* ^{121}Sb Mössbauer spectroscopy is not sensitive enough to contribute to the identification of these phases obtained at the end of the discharge and charge processes (cf. Supplementary Material).

EXAFS, on the other hand, becomes much more helpful when one looks at the intermediate phases. Indeed, during the first discharge, two different intermediate components appear simultaneously with different intensities. The first one, the only intermediate clearly visible from the Bi side, is represented by a ternary Na-Bi-Sb compound, which is likely the crystalline intermediate also detected by XRD. The second one, on the other hand, is visible only from the Sb side and is clearly a Bi-free Sb-rich sodiated intermediate either represented by a composition similar to *BiSb*, or to a mixture of pure Sb and of Na_3Sb. Similar Na-Sb intermediate species, amorphous in nature, could be observed by PDF in the sodiation of pure Sb but were not detected by XRD [92]. The same two components appear again, even though with reversed intensities, during the following charge from the decomposition of $Na_3(Bi_{0.50}Sb_{0.50})$, suggesting an increased segregation of Sb and Bi along cycling. Interestingly, the segregation is probably not extended to the formation of long-range ordered Sb-Na species, since the ternary $Na_3(Bi_{0.50}Sb_{0.50})$ is reformed again at the end of the second discharge, as detected by XRD. It is unfortunate that the XAS experiment had to be stopped in the middle of the charge due to technical problems at the beamline, but the collected spectra are sufficient to highlight the clear modification of the spectra in the middle of the charge compared to the middle of the discharge.

On the basis of these observation, and taking into account the compositions of the different intermediates identified by EXAFS and XRD, one can propose a overall cycling mechanism for *BiSb* (the prefix (*a*) stands for amorphous):

- 1st discharge

$$Bi_{0.5}Sb_{0.5} \rightarrow (a)Na_yBi_{1-x}Sb_x + (a)Na_zSb \rightarrow Na_3Bi_{0.50}Sb_{0.50} \quad (3)$$

- 1st charge

$$Na_3Bi_{0.50}Sb_{0.50} \rightarrow Na_yBi_{1-x}Sb_x + (a)Na_zSb \rightarrow Bi_{0.5}Sb_{0.5} + 3Na \quad (4)$$

Upon cycling, a gradual decrease of the capacity is observed, strongly dependent on the amount of bismuth. The observed increase of the segregation between the first discharge and the following charge suggests a gradual segregation of the two metals upon cycling. The poor performance of Bi, probably due to stronger electrolyte degradation than for Sb, might be then the cause of rapid capacity fading.

4. Conclusion

In the last decade, a strong activity on the application of *operando* XAS to the characterisation of battery and battery materials has been developed at ICGM. Different families of electrode materials and battery systems, going from insertion to conversion materials for LIB, to LIS systems, to Sb-based alloy materials for NIB. In all these systems, XAS has played a major role for the determination of the cycling mechanism, in particular when the electrode materials went through extensive nanostructuring and/or amorphisation.

The capabilities of XAS where evidently demonstrated in the example of the study of Bi-Sb alloy materials, where its contribution for the understanding of the mechanism is strongly complementary to that of XRD. The importance of XAS in this particular experiment is even more important considering the highly challenging experimental conditions that had to be set for collecting simultaneously *operando* Sb K-edge and Bi L_3-edge XAS spectra on the same cycling cell.

Acknowledgements

Thanks to all concerned beamlines and scientists. Thanks to Alistore for the post-doc grant of MF. The research on Li-sulfur batteries received funding from the European Union Seventh Framework Programme under the grant agreement 314515 (EUROLIS). Research sponsored by the Laboratory Directed Research and Development Program of Oak Ridge National Laboratory, managed by UT-Battelle, LLC, for the U.S. Department of Energy. Synchrotron SOLEIL (France) is gratefully acknowledged for providing beamtime at the ROCK beamline (financed by the French National Research Agency as part of the *Investissements d'Avenir* programme, reference ANR-10-EQPX-45). The research group Catalyse, Réactivité de Surface et Rayonnement Synchrotron (GDR CNRS 3590) is gratefully acknowledged for its information and supporting activity for the application of the chemometric approach in the analysis of spectroscopic data.

Appendix A. Supplementary data

Supplementary data to this article can be found online at https://doi.org/10.1016/j.ensm.2019.06.027.

References

[1] B. Dunn, H. Kamath, J.-M. Tarascon, Science 334 (2011) 928–935, https://doi.org/10.1126/science.1212741.
[2] M. Armand, J.-M. Tarascon, Nature 451 (2008) 652–657, https://doi.org/10.1038/451652a.
[3] M. Wagemaker, F.M. Mulder, Acc. Chem. Res. 46 (2013) 1206–1215, https://doi.org/10.1021/ar2001793.
[4] C. Masquelier, L. Croguennec, Chem. Rev. 113 (2013) 6552–6591, https://doi.org/10.1021/cr3001862.
[5] M.S. Whittingham, Chem. Rev. 104 (2004) 4271–4302.
[6] M.N. Obrovac, V.L. Chevrier, Chem. Rev. 114 (2014) 11444–11502, https://doi.org/10.1021/cr500207g.
[7] H. Kim, G. Jeong, Y.-U. Kim, J.-H. Kim, C.-M. Park, H.-J. Sohn, Chem. Soc. Rev. 42 (2013) 9011–9034, https://doi.org/10.1039/c3cs60177c.
[8] C.-M. Park, J.-H. Kim, H. Kim, H.-J. Sohn, Chem. Soc. Rev. 39 (2010) 3115–3141, https://doi.org/10.1039/b919877f.
[9] J. Cabana, L. Monconduit, D. Larcher, M.R. Palacín, Adv. Mater. 22 (2010) E170–E192.
[10] S.-H. Yu, X. Feng, N. Zhang, J. Seok, H.D. Abruña, Acc. Chem. Res. 51 (2018) 273–281, https://doi.org/10.1021/acs.accounts.7b00487.
[11] A. Kraytsberg, Y. Ein-Eli, J. Solid State Electrochem. 21 (2017) 1907–1923, https://doi.org/10.1007/s10008-017-3580-9.

[12] F. Wu, G. Yushin, Energy Environ. Sci. 10 (2017) 435–459, https://doi.org/10.1039/C6EE02326F.
[13] E. Peled, J. Electrochem. Soc. 126 (1979) 2047–2051, https://doi.org/10.1149/1.2128859.
[14] D. Alves Dalla Corte, G. Caillon, C. Jordy, J.-N. Chazalviel, M. Rosso, F. Ozanam, Adv. Energy Mater. 6 (2016) 1501768, https://doi.org/10.1002/aenm.201501768.
[15] A.M. Tripathi, W.-N. Su, B.J. Hwang, Chem. Soc. Rev. 47 (2018), https://doi.org/10.1039/C7CS00180K, 736–851.
[16] C. Marino, A. Boulaoued, J. Fullenwarth, D. Maurin, N. Louvain, J.-L. Bantignies, L. Stievano, L. Monconduit, J. Phys. Chem. C 121 (2017) 26598–26606, https://doi.org/10.1021/acs.jpcc.7b06685.
[17] Y. Deng, S. Dong, Z. Li, H. Jiang, X. Zhang, X. Ji, Small Methods 2 (2018) 1700332, https://doi.org/10.1002/smtd.201700332.
[18] R. Baddour-Hadjean, J.-P. Pereira-Ramos, Chem. Rev. 110 (2010) 1278–1319.
[19] J. Hannauer, J. Scheers, J. Fullenwarth, B. Fraisse, L. Stievano, P. Johansson, ChemPhysChem 16 (2015) 2755–2759, https://doi.org/10.1002/cphc.201500708.
[20] P.-E. Lippens, J.-C. Jumas, Mössbauer Effect Ref. Data J. 33 (2010) 31.
[21] M. Balasubramanian, X. Sun, X.Q. Yang, J. McBreen, J. Power Sources 92 (2001) 1–8, https://doi.org/10.1016/S0378-7753(00)00493-6.
[22] P. Shearing, Y. Wu, S.J. Harris, N. Brandon, Interface 20, 2011, pp. 43–47, http://www.electrochem.org/dl/interface/fal/fal11/fal11{_}p043-047.pdf.
[23] J.R. Croy, M. Balasubramanian, D. Kim, S.-H. Kang, M.M. Thackeray, Chem. Mater. 23 (2011) 5415–5424, https://doi.org/10.1021/cm2026703.
[24] Q. Li, R. Qiao, L.A. Wray, J. Chen, Z. Zhuo, Y. Chen, S. Yan, F. Pan, Z. Hussain, W. Yang, J. Phys. D Appl. Phys. 49 (2016) 413003, https://doi.org/10.1088/0022-3727/49/41/413003. http://stacks.iop.org/0022-3727/49/i=41/a=413003?.
[25] M. Giorgetti, L. Stievano, in: M. Khodaei, L. Petaccia (Eds.), X-ray Characterization of Nanostructured Energy Materials by Synchrotron Radiation, 1 ed., InTech, Rijeka, 2017, pp. 51–75, https://doi.org/10.5772/66868.
[26] W. Li, M. Li, Y. Hu, J. Lu, A. Lushington, R. Li, T. Wu, T.-K. Sham, X. Sun, Small Methods 2 (2018) 1700341, https://doi.org/10.1002/smtd.201700341.
[27] S.K. Martha, E. Markevich, V. Burgel, G. Salitra, E. Zinigrad, B. Markovsky, H. Sclar, Z. Pramovich, O. Heik, D. Aurbach, I. Exnar, H. Buqa, T. Drezen, G. Semrau, M. Schmidt, D. Kovacheva, N. Saliyski, J. Power Sources 189 (2009) 288–296, https://doi.org/10.1016/j.jpowsour.2008.09.084.
[28] P. Verma, P. Maire, P. Novák, Electrochim. Acta 55 (2010) 6332–6341, https://doi.org/10.1016/j.electacta.2010.05.072.
[29] N. Sharma, W.K. Pang, Z. Guo, V.K. Peterson, ChemSusChem 8 (2015) 2826–2853, https://doi.org/10.1002/cssc.201500152.
[30] J. Yang, S. Muhammad, M.R. Jo, H. Kim, K. Song, D.A. Agyeman, Y.-I. Kim, W.-S. Yoon, Y.-M. Kang, Chem. Soc. Rev. 45 (2016) 5717–5770, https://doi.org/10.1039/C5CS00734H.
[31] M. Fehse, M.T. Sougrati, A. Darwiche, V. Gabaudan, C. La Fontaine, L. Monconduit, L. Stievano, J. Mater. Chem. A 6 (2018) 8724–8734, https://doi.org/10.1039/C8TA02248H.
[32] J.-B. Leriche, S. Hamelet, J. Shu, M. Morcrette, C. Masquelier, G. Ouvrard, M. Zerrouki, P. Soudan, S. Belin, E. ElkaÃŕm, F. Baudelet, J. Electrochem. Soc. 157 (2010) A606–A610, https://doi.org/10.1149/1.3355977.
[33] J. McBreen, W.E. O'Grady, K.I. Pandya, J. Power Sources 22 (1988) 323–340, https://doi.org/10.1016/0378-7753(88)80027-2.
[34] V. Briois, C. La Fontaine, S. Belin, L. Barthe, T. Moreno, V. Pinty, A. Carcy, R. Girardot, E. Fonda, J. Phys. Conf. Ser. 712 (2016) 012149, https://doi.org/10.1088/1742-6596/712/1/012149.
[35] X. Carrier, E. Marceau, H. Carabineiro, V. Rodríguez-González, M. Che, Phys. Chem. Chem. Phys. 11 (2009) 7527, https://doi.org/10.1039/b822969d.
[36] J. Singh, C. Lamberti, J.A. van Bokhoven, Chem. Soc. Rev. 39 (2010) 4754–4766, https://doi.org/10.1039/c0cs00054j.
[37] D. Ferri, M.A. Newton, M. Nachtegaal, Top. Catal. 54 (2011) 1070–1078.
[38] A.I. Frenkel, Chem. Soc. Rev. 41 (2012) 8163–8178, https://doi.org/10.1039/c2cs35174a.
[39] J.A. van Bokhoven, C. Lamberti, X-ray Absorption and X-ray Emission Spectroscopy : Theory and Applications, John Wiley & Sons Ltd., Chichester, UK, 2016. http://eu.wiley.com/WileyCDA/WileyTitle/productCd-1118844238.html.
[40] E.I. Solomon, Coord. Chem. Rev. 249 (2005) 1–2, https://doi.org/10.1016/j.ccr.2004.04.003.
[41] I. Ascone, R. Fourme, S.S. Hasnain, J. Synchrotron Radiat. 10 (2003) 1–3, https://doi.org/10.1107/S0909049502022434.
[42] R.C. Nelson, J.T. Miller, Catal. Sci. Technol. 2 (2012) 461–470, https://doi.org/10.1039/C2CY00343K.
[43] F. Boscherini, in: C.M. Settimio Mobilio, Federico Boscherini (Eds.), Synchrotron Radiation, Springer Berlin Heidelberg, Berlin, Heidelberg, 2015, pp. 485–498, https://doi.org/10.1007/978-3-642-55315-8_17.
[44] H.D. Dewald, Electroanalysis 3 (1991) 145–155, https://doi.org/10.1002/elan.1140030303.
[45] B.K. Teo, EXAFS: Basic Principles and Data Analysis, Volume 9 of Inorganic Chemistry Concepts, Springer Berlin Heidelberg, Berlin, Heidelberg, Germany, 1986, https://doi.org/10.1007/978-3-642-50031-2.
[46] D.C. Koningsberger, R. Prins, X-ray Absorption : Principles, Applications, Techniques of EXAFS, SEXAFS, and XANES, Wiley Interscience, New York, USA, 1988. http://eu.wiley.com/WileyCDA/WileyTitle/productCd-0471875473.html.
[47] G. Bunker, Introduction to XAFS, A Practical Guide to X-ray Absorption Fine Structure Spectroscopy, Cambridge University Press, Cambridge, UK, 2010. https://www.cambridge.org/fr/academic/subjects/physics/condensed-matter-physics-nanoscience-and-mesoscopic-physics/introduction-xafs-practical-guide-x-ray-absorption-fine-structure-spectroscopy.
[48] A. Darwiche, M. Fehse, A. Mahmoud, C.L. Fontaine, B. Fraisse, R. Hermann, M.-L. Doublet, L. Monconduit, M.T. Sougrati, M. Ben Yahia, L. Stievano, Batteries 4 (2018) 25, https://doi.org/10.3390/BATTERIES4020025.
[49] M. Morcrette, Y. Chabre, G.B.M. Vaughan, G.G. Amatucci, J.-B. Leriche, S. Patoux, C. Masquelier, J.-M. Tarascon, Electrochim. Acta 47 (2002) 3137–3149, https://doi.org/10.1016/S0013-4686(02)00233-5.
[50] M. Ati, M.T. Sougrati, N. Recham, P. Barpanda, J.-B. Leriche, M. Courty, M. Armand, J.-C. Jumas, J.-M. Tarascon, J. Electrochem. Soc. 157 (2010) A1007–A1015, https://doi.org/10.1149/1.3457435.
[51] J.-C. Jumas, L. Stievano, M.T. Sougrati, J. Fullenwarth, B. Fraisse, J.-B. Leriche, Analysis of the Features of an Electrode Material of an Electrochemical Cell, 2014. https://patents.google.com/patent/WO2014033402A1/.
[52] A. Perea, L. Castro, L. Aldon, L. Stievano, R. Dedryvère, D. Gonbeau, N. Tran, G. Nuspl, J. Bréger, C. Tessier, J. Solid State Chem. 192 (2012) 201–209, https://doi.org/10.1016/j.jssc.2012.04.016.
[53] A. Iadecola, A. Perea, L. Aldon, G. Aquilanti, L. Stievano, J. Phys. D Appl. Phys. 50 (2017) 144004, https://doi.org/10.1088/1361-6463/aa605c.
[54] R. Tauler, Chemometr. Intell. Lab. 30 (1995) 133–146, https://doi.org/10.1016/0169-7439(95)00047-X.
[55] A. de Juan, J. Jaumot, R. Tauler, Anal. Methods 6 (2014) 4964, https://doi.org/10.1039/c4ay00571f.
[56] W.H. Cassinelli, L. Martins, A.R. Passos, S.H. Pulcinelli, C.V. Santilli, A. Rochet, V. Briois, Catal. Today 229 (2014) 114–122, https://doi.org/10.1016/j.cattod.2013.10.077.
[57] M. Fehse, A. Iadecola, M.T. Sougrati, P. Conti, M. Giorgetti, L. Stievano, Energy Storage Mater. 18, 2019, pp. 328–337, https://doi.org/10.1016/j.ensm.2019.02.002.
[58] C. Lesage, E. Devers, C. Legens, G. Fernandes, O. Roudenko, V. Briois, Catal. Today (2019), https://doi.org/10.1016/j.cattod.2019.01.081 doi:10.1016/j.cattod.2019.01.081.
[59] M. Fehse, F. Fischer, C. Tessier, L. Stievano, L. Monconduit, J. Power Sources 231 (2013) 23–28, https://doi.org/10.1016/j.jpowsour.2012.12.058.
[60] M. Fehse, E. Ventosa, ChemPlusChem 80 (2015) 785–795, https://doi.org/10.1002/cplu.201500038.
[61] M. Fehse, L. Monconduit, F. Fischer, C. Tessier, L. Stievano, Solid State Ionics 268 (2014a) 252–255, https://doi.org/10.1016/j.ssi.2014.09.018.
[62] M. Fehse, M. Ben Yahia, L. Monconduit, F. Lemoigno, M.-L. Doublet, F. Fischer, C. Tessier, L. Stievano, J. Phys. Chem. C 118 (2014b) 27210–27218, https://doi.org/10.1021/jp507574e.
[63] M. Giorgetti, A. Mignani, G. Aquilanti, P. Conti, M. Fehse, L. Stievano, J. Phys. Conf. Ser. 712 (2016) 012127, https://doi.org/10.1088/1742-6596/712/1/012127.
[64] A. Mullaliu, M.T. Sougrati, N. Louvain, G. Aquilanti, M.-L. Doublet, L. Stievano, M. Giorgetti, Electrochim. Acta 257 (2017) 364–371, https://doi.org/10.1016/j.electacta.2017.10.107.
[65] A. Mullaliu, P. Conti, G. Aquilanti, J. Plaisier, L. Stievano, M. Giorgetti, Condens. Matter 3 (2018a) 36, https://doi.org/10.3390/condmat3040036.
[66] A. Mullaliu, G. Aquilanti, P. Conti, J.R. Plaisier, M. Fehse, L. Stievano, M. Giorgetti, J. Phys. Chem. C 122 (2018b) 15868–15877, https://doi.org/10.1021/acs.jpcc.8b03429.
[67] P.G. Bruce, S.A. Freunberger, L.J. Hardwick, J.-M. Tarascon, Nat. Mater. 11 (2011) 19–29, https://doi.org/10.1038/nmat3191.
[68] A. Manthiram, Y. Fu, S.-H. Chung, C. Zu, Y.-S. Su, Chem. Rev. 114 (2014) 11751–11787, https://doi.org/10.1021/cr500062v.
[69] Y.V. Mikhaylik, J.R. Akridge, J. Electrochem. Soc. 150 (2003) A306–A311, https://doi.org/10.1149/1.1545452.
[70] S.-E. Cheon, K.-S. Ko, J.-H. Cho, S.-W. Kim, E.-Y. Chin, H.-T. Kim, J. Electrochem. Soc. 150 (2003a) A800–A805, https://doi.org/10.1149/1.1571533.
[71] S.-E. Cheon, K.-S. Ko, J.-H. Cho, S.-W. Kim, E.-Y. Chin, H.-T. Kim, J. Electrochem. Soc. 150 (2003b) A796–A799, https://doi.org/10.1149/1.1571532.
[72] N.-S. Choi, Z. Chen, S.A. Freunberger, X. Ji, Y.-K. Sun, K. Amine, G. Yushin, L.F. Nazar, J. Cho, P.G. Bruce, Angew. Chem. Int. Ed. 51 (2012) 9994–10024, https://doi.org/10.1002/anie.201201429.
[73] Q. Pang, X. Liang, C.Y. Kwok, L.F. Nazar, J. Electrochem. Soc. 162 (2015) A2567–A2576, https://doi.org/10.1149/2.0171514jes.
[74] Q. Pang, X. Liang, C.Y. Kwok, L.F. Nazar, Nature Energy 1 (2016) 16132, https://doi.org/10.1038/nenergy.2016.132.
[75] R. Fang, S. Zhao, Z. Sun, D.-W. Wang, H.-M. Cheng, F. Li, Adv. Mater. 29 (2017) 1606823, https://doi.org/10.1002/adma.201606823.
[76] Y. He, Z. Chang, S. Wu, H. Zhou, J. Mater. Chem. A 6 (2018) 6155–6182, https://doi.org/10.1039/C8TA01115J.
[77] M. Wild, L. O'Neill, T. Zhang, R. Purkayastha, G. Minton, M. Marinescu, G.J. Offer, Energy Environ. Sci. 8 (2015) 3477–3494, https://doi.org/10.1039/C5EE01388G.
[78] M.U.M. Patel, I. Arčon, G. Aquilanti, L. Stievano, G. Mali, R. Dominko, ChemPhysChem 15 (2014) 894–904, https://doi.org/10.1002/cphc.201300972.
[79] R. Dominko, M.U.M. Patel, V. Lapornik, A. Vizintin, M. Koželj, N. Novak Tušar, I. Arcon, L. Stievano, G. Aquilanti, J. Phys. Chem. C 119 (2015) 19001–19010, https://doi.org/10.1021/acs.jpcc.5b05609.
[80] G. Aquilanti, M. Giorgetti, R. Dominko, L. Stievano, I. Arčon, N. Novello, L. Olivi, J. Phys. D Appl. Phys. 50 (2017) 074001, https://doi.org/10.1088/1361-6463/aa519a.

[81] A. Vizintin, L. Chabanne, E. Tchernychova, I. Arčon, L. Stievano, G. Aquilanti, M. Antonietti, T.-P. Fellinger, R. Dominko, J. Power Sources 344 (2017) 208–217, https://doi.org/10.1016/j.jpowsour.2017.01.112.
[82] R. Dominko, A. Vizintin, G. Aquilanti, L. Stievano, M.J. Helen, A.R. Munnangi, M. Fichtner, I. Arcon, J. Electrochem. Soc. 165 (2018) A5014–A5019, https://doi.org/10.1149/2.0151801jes.
[83] C. Villevieille, B. Fraisse, M. Womes, J.-C. Jumas, L. Monconduit, J. Power Sources 189 (2009) 324–330, https://doi.org/10.1016/j.jpowsour.2008.08.089.
[84] C. Villevieille, C.M. Ionica-Bousquet, B. Ducourant, J.-C. Jumas, L. Monconduit, J. Power Sources 172 (2007) 388–394, https://doi.org/10.1016/j.jpowsour.2007.06.256.
[85] C. Marino, B. Fraisse, M. Womes, C. Villevieille, L. Monconduit, L. Stievano, J. Phys. Chem. C 118 (2014) 27772–27780, https://doi.org/10.1021/jp5097579.
[86] M. Fehse, A. Darwiche, M.T. Sougrati, E.M. Kelder, A.V. Chadwick, M. Alfredsson, L. Monconduit, L. Stievano, Chem. Mater. 29 (2017) 10446–10454, https://doi.org/10.1021/acs.chemmater.7b04088.
[87] M.T. Sougrati, J. Fullenwarth, A. Debenedetti, B. Fraisse, J.-C. Jumas, L. Monconduit, J. Mater. Chem. 21 (2011) 10069, https://doi.org/10.1039/c1jm10710k.
[88] H. Wilhelm, C. Marino, A. Darwiche, L. Monconduit, B. Lestriez, Electrochem. Commun. 24 (2012) 89–92, https://doi.org/10.1016/j.elecom.2012.08.023.
[89] A. Darwiche, C. Marino, M.T. Sougrati, B. Fraisse, L. Stievano, L. Monconduit, J. Am. Chem. Soc. 134 (2012) 20805–20811, https://doi.org/10.1021/ja310347x.
[90] A. Darwiche, M.T. Sougrati, B. Fraisse, L. Stievano, L. Monconduit, Electrochem. Commun. 32 (2013) 18–21, https://doi.org/10.1016/j.elecom.2013.03.029.
[91] A. Darwiche, M. Toiron, M.T. Sougrati, B. Fraisse, L. Stievano, L. Monconduit, J. Power Sources 280 (2015) 588–592, https://doi.org/10.1016/j.jpowsour.2015.01.138.
[92] P.K. Allan, J.M. Griffin, A. Darwiche, O.J. Borkiewicz, K.M. Wiaderek, K.W. Chapman, A.J. Morris, P.J. Chupas, L. Monconduit, C.P. Grey, J. Am. Chem. Soc. 138 (2016) 2352–2365, https://doi.org/10.1021/jacs.5b13273.
[93] M. Fehse, D. Bessas, A. Darwiche, A. Mahmoud, G. Rahamim, C. La Fontaine, R.P. Hermann, D. Zitoun, L. Monconduit, L. Stievano, M.T. Sougrati, Batteries Supercaps 2 (2019) 66–73, https://doi.org/10.1002/batt.201800075.
[94] F. Murgia, D. Laurencin, E.T. Weldekidan, L. Stievano, L. Monconduit, M.-L. Doublet, R. Berthelot, Electrochim. Acta 259 (2018) 276–283, https://doi.org/10.1016/j.electacta.2017.10.170.
[95] V. Gabaudan, R. Berthelot, L. Stievano, L. Monconduit, J. Phys. Chem. C 122 (2018) 18266–18273, https://doi.org/10.1021/acs.jpcc.8b04575.
[96] W.F. Ehret, M.B. Abramson, J. Am. Chem. Soc. 56 (1934) 385–388, https://doi.org/10.1021/ja01317a031.
[97] B. Lenoir, M. Cassart, J.-P. Michenaud, H. Scherrer, S. Scherrer, J. Phys. Chem. Solids 57 (1996) 89–99, https://doi.org/10.1016/0022-3697(95)00148-4.
[98] H. Kitagawa, H. Noguchi, T. Kiyabu, M. Itoh, Y. Noda, J. Phys. Chem. Solids 65 (2004) 1223–1227, https://doi.org/10.1016/j.jpcs.2004.01.010.
[99] D. Hsieh, D. Qian, L. Wray, Y. Xia, Y.S. Hor, R.J. Cava, M.Z. Hasan, Nature 452 (2008) 970–974, https://doi.org/10.1038/nature06843.
[100] G.D. Zally, J.M. Mochel, Phys. Rev. Lett. 27 (1971) 1710–1712, https://doi.org/10.1103/PhysRevLett.27.1710.
[101] Y.-M. Lin, O. Rabin, S.B. Cronin, J.Y. Ying, M.S. Dresselhaus, Appl. Phys. Lett. 81 (2002) 2403–2405, https://doi.org/10.1063/1.1503873.
[102] X. Li, J. Ni, S.V. Savilov, L. Li, Chem. Eur J. 24 (2018) 13719–13727, https://doi.org/10.1002/chem.201801574.
[103] Y. Zhao, A. Manthiram, Chem. Mater. 27 (2015) 3096–3101, https://doi.org/10.1021/acs.chemmater.5b00616.
[104] H. Xie, W.P. Kalisvaart, B.C. Olsen, E.J. Luber, D. Mitlin, J.M. Buriak, J. Mater. Chem. A 5 (2017) 9661–9670, https://doi.org/10.1039/C7TA01443K.
[105] T.S. Arthur, N. Singh, M. Matsui, Electrochem. Commun. 16 (2012) 103–105, https://doi.org/10.1016/j.elecom.2011.12.010.
[106] H. Berger, B. Christ, J. Troschke, Cryst. Res. Technol. 17 (1982) 1233–1239, https://doi.org/10.1002/crat.2170171010.